Numerical prediction of the effect of irradiation on the Charpy Upper Shelf Energy of Reactor Pressure Vessel steels

Jeremy Hure, Aurore Parrot, Sébastien Meunier

Numerical prediction of the effect of irradiation on the Charpy Upper Shelf Energy of Reactor Pressure Vessel steels

J. Hure[a,1], A. Parrot[b], S. Meunier[b]

[a]*Université Paris-Saclay, CEA, Service d'Étude des Matériaux Irradiés, 91191, Gif-sur-Yvette, France*
[b]*EDF R&D, Site des Renardières, 77818 Moret-sur-Loing, France*

Abstract

Neutron irradiation affects the mechanical properties of Reactor Pressure Vessel (RPV) steels used in Light Water Reactors (LWR). Fracture properties are particularly monitored based on surveillance programs, mostly through Charpy impact tests. The evolutions of Ductile Brittle Transition Temperature (DBTT) and Upper Shelf Energy (USE) with irradiation are evaluated and used for structural integrity assessment depending on regulation procedures. Semi-empirical correlations have been proposed to predict DBTT and USE shifts as a function of material chemical composition and fast neutron fluence, based on extended experimental database. In this study, numerical simulations of Charpy impact tests are performed in order to predict quantitatively the evolution of USE with irradiation. In a first part, the mechanical properties of an A508 Cl3 RPV steel are presented, including tensile tests on flat and notched samples and Charpy impact tests, for various irradiation levels and test temperatures. USE values are found to be within the bounds of correlation curves. In a second part, the experimental data are used to calibrate constitutive equations describing the material behavior up to high strain levels. Charpy impact test finite element simulations are then detailed, including ductile fracture modelling. In a third part, the ductile fracture model is calibrated based on the experimental data, and numerical simulations are used to predict the evolution of USE with irradiation. The decrease of USE with irradiation is recovered, and the numerical results are found to be in quantitative agreement with the correlation curves. Additional simulations confirm the agreement for different reference unirradiated USE and chemical composition, as well as using a simplified ductile fracture model. These results indicate that numerical simulations of Charpy impact test relying on calibrated constitutive equations can be used to predict USE and required experimental characterization are finally discussed.

Keywords: Reactor Pressure Vessel, Neutron irradiation, Fracture properties, Charpy impact test, Upper Shelf Energy

1. Introduction

Reactor Pressure Vessel (RPV) of Light Water Reactors (LWR) are made of low alloy steels such as A508 for modern LWRs [1]. These ferritic steels exhibit a ductile brittle transition [2]. Well below the Ductile Brittle Transition Temperature (DBTT), brittle fracture occurs through cleavage [3] and the associated fracture energy is low. Well above the DBTT, ductile fracture occurs through nucleation, growth and coalescence [4] of internal voids associated with high fracture energy. The operating temperature of LWRs ($\sim 290°C$) is well above the DBTT for A508 steels at the beginning of operation. However, neutron irradiation leads to an upward shift of the DBTT [1], thus requiring monitoring through dedicated surveillance programs [5, 6] for structural integrity assessment. Neutron embrittlement of RPV steels can be assessed through impact tests on Charpy V-Notch (CVN) specimens or fracture toughness tests on pre-cracked specimens. In the latter and historically newer approach, quasi-static isothermal tests are performed and analyzed based on the Master Curve approach [7], leading to the evaluation of the reference temperature T_0 characterizing the ductile brittle transition. A review of the application of the Master Curve approach to the neutron embrittlement of RPV steels can be found in [8]. In the former, index temperature corresponding to a given CVN fracture energy T_X (typically $X = 41$J or 56J) and Upper Shelf Energy (USE) are quantified. Index temperatures are used to evaluate the shift of DBTT $\Delta T = \Delta T_X$ (or ΔT_0) while USE gives the fracture energy at LWR operating temperature. In surveillance programs [6], ΔT is used to update the lower bound toughness curve used to assess structural integrity, while tests on fracture toughness specimens are used to evaluate the conservatism of the approach. ΔT and USE depend on both irradiation conditions (fast neutron fluence, temperature) and chemical composition of the material. Various analytical models, loosely referred to as Embrittlement Trend Curves (ETC) in the following, have been proposed to predict the temperature shift ΔT. Statistical analysis of extended experimental database leads to NUREG-6551 [9] and FIM [10] semi-empirical correlations, based on US and France data, respectively. Physically-based correlations have also been proposed, such as the JEAC4201 model relying on the quantification of irradiation defects [11] or the EONY model [12]. The reader is referred to the thorough review on ETC development and current status [13]. Fewer models have been proposed to predict the decrease of USE with irradiation. In addition to ΔT prediction, NUREG-6551 [9] proposed a model for the USE that depends on neutron fluence, chemical composition and product form (welds, plates, forgings). Later on, additional correlations have been proposed [14, 15] based on regression analysis of experimental data. While previous correlations have been developed independently of ΔT correlations, UNM-6 model [16] is based on the linear relation between ΔUSE and ΔT, further

*Corresponding author: jeremy.hure@cea.fr

discussed in [17] by pointing out a direct relationship between T_{41J} and USE. A simple model has been proposed recently depending solely on copper content and fast neutron fluence [18]. All USE correlations provide satisfactory agreement with respect to experimental data, owing to the large scatter. NUREG-6551 [9] and UNM-6 [16] predictions have been compared in [19] to experimental data from Belgian surveillance program. Large scatter is observed, but the UNM-6 model was shown to be in better agreement with that specific set of data.

Neutron embrittlement of western RPV steels is due to irradiation-induced hardening resulting from the presence of solute clusters and matrix defects [1, 20]. Non-hardening embrittlement related to segregation of alloying elements like phosphorus at grain boundaries under irradiation can be observed in specific conditions, *i.e.*, VVER RPV steels [21], which are not considered here. Hence evolutions of macroscopic fracture properties measured on impact and toughness tests (T_0, T_X, USE) are directly related to the increase of hardening, as used explicitly in JEAC4201 and EONY models to predict ΔT. Numerous studies have been performed dealing with the evolution of fracture toughness with irradiation in the brittle regime [22, 23]. Brittle fracture of RPV steels is commonly described using Beremin-like models [24, 25] requiring analytical or numerical estimation of local stress / strain fields. The main input parameters are the stress-strain curves and the local fracture properties - calibrated at the reference state - and the output is the shift of the reference temperature T_0. Details and current status of this approach can be found in papers related to recent European projects on the topic [26, 27]. Less work has been done to predict the evolution of Charpy impact tests fracture properties (T_{XJ}, USE) with irradiation using numerical simulations. In addition to stress-strain curves and cleavage fracture model for the brittle regime, these simulations require accurate modeling of ductile fracture. Physically-based modelling of ductile fracture through void growth to coalescence relies on dedicated constitutive equations where void volume fraction / porosity is included as a state variable. Based on the homogenization of a hollow sphere, Gurson proposed a yield criterion for porous materials [28], relevant to ductile fracture. The model was later improved by Tvergaard and Needleman and is referred to as the GTN model which is still widely used nowadays [29, 30]. Since then, refined models have been proposed accounting for increasing complexity - anisotropy, void shape - and the reader is referred to the recent reviews on the topic [31, 32]. These ductile fracture constitutive equations are used to perform finite element ductile tearing simulations. Pioneered by Norris [33], Charpy V-Notch finite element simulations including ductile tearing have been improved over the years [34, 35, 36] to include 3D effects and detailed comparisons to experimental data. CVN simulations have then been applied to predict the neutron embrittlement of RPV steels. Early studies [37, 38] combined Beremin-like model to predict brittle fracture and GTN-like ductile model for stable crack growth in order to predict the shift of ductile brittle transition curves with irradiation. These studies were later refined in [39, 40] to predict (ΔT_{XJ}, ΔUSE).

All these studies pave the way towards quantitative prediction of the neutron embrittlement of RPV steel through a multi-scale approach, removing the need for semi-empirical correlations. In a nutshell, physically-based models predict irradiation-induced defects and their effect on hardening as a function of material chemical composition and fast neutron fluence. Numerical simulations using relevant fracture models can then predict the evolution of fracture properties accounting for irradiation-induced hardening. However, as shown in [39], such approach requires accurate constitutive equations to model the material behavior as well as accurate brittle and ductile fracture models. First, experimental data characterizing large deformation behavior of RPV steels are necessary to go beyond *ad hoc* hypotheses often made in the literature (power-law hardening calibrated at small strains extended to large strains, assumptions regarding the effect of irradiation on hardening [39]). Typically, tensile tests on notched samples or torsion tests allow assessing large strains [41] and are widely used for unirradiated material. Experimental data remains however scarce for irradiated RPV steels [42], especially regarding the effect of irradiation level. Secondly, fracture models, either brittle or ductile, have parameters requiring calibration. In particular, the dependence of these parameters to the irradiation level is still an open question, for both brittle [43] and ductile [44] fracture. Predicting the shift of index temperature ΔT_X is a challenging task as stable ductile crack growth can appear before unstable brittle failure, thus requiring brittle and ductile fracture modelling. The prediction of the evolution of upper shelf energy with irradiation may be simpler as only ductile failure is involved, but barely no numerical predictions has been proposed so far [39]. Therefore, the aim of this study is to perform numerical simulations of Charpy impact tests of RPV steels and to predict the effect of irradiation on the upper shelf energy. The paper is organized as follows. In a first part, an experimental database on unirradiated and irradiated RPV steel is first presented, including a thorough assessment of strain-hardening behavior for high strains - relevant for ductile fracture modelling - as a function of irradiation fluence and temperature. In a second part, the constitutive equations used to model strain-hardening are detailed and calibrated based on the experimental data. The ductile fracture model is then described as well as the Charpy impact test simulations. In a third part, the full model is calibrated with respect to experimental Charpy load-displacement curves. The numerical prediction of the effect of irradiation on upper shelf energy is described and compared to the correlations available in the literature. Finally, the effects of material parameters and of the choice of the ductile fracture model are discussed.

2. Experimental characterization

In this section, an experimental characterization of a RPV steel is presented, focusing on the effects of irradiation on both mechanical behavior measured by tensile tests on smooth and notched specimens and upper shelf energy measured through Charpy impact tests.

2.1. Materials

The materials considered in this study are A508 Cl3 steel referred to as 16MND5 in France [6]. Two different materials are used with slight differences of chemical composition, as shown in Tab. 1. The main difference is related

to the phosphorus content known to affect irradiation-induced hardening and embrittlement. Both materials were heat treated (two austenizing treatments followed by water quenching and tempering, and a final stress relief treatment). The associated microstructure is a tempered bainite.

	C	S	P	Mn	Si	Ni	Cr	Mo	V	Cu	Co	Al
Material #1	0.14	0.004	0.006	1.33	0.19	0.73	0.21	0.49	<0.01	0.06	0.02	0.025
Material #2	0.15	0.006	0.013	1.31	0.22	0.70	0.19	0.52	<0.01	0.07	0.02	0.022

Table 1: Chemical composition (weight %) of the materials

The Material #1 is used for the characterization of the mechanical behavior and has been irradiated as part of EDF surveillance program to different levels of fast neutron fluence [6]. The Material #2 originating from a forged nozzle shell is used for the evolution of the upper shelf energy with irradiation. It has been irradiated in the Material Testing Reactors Osiris (CEA Saclay) and RBT-6 (RIAR) to different fast neutron fluences. Experimental characterization and modelling on Material #2 have been reported in previous studies [42, 45]. The irradiation conditions are summarized in Tab. 2.

	Irradiation temperature (°C)	**Flux (E>1MeV)** (10^{12}n.cm^{-2}.s^{-1})	**Fluence (E>1MeV)** (10^{19}n.cm^{-2})
Material #1	~ 288	~ 0.2	[0 - 7.5]
Material #2		~ 5	[0 - 14]

Table 2: Irradiation conditions of the materials: Material #1 has been irradiated as part of the EDF surveillance program [6], Material #2 has been irradiated in MTRs [42, 45]

In the range considered in Tab. 2, fast neutron flux has been shown to have a negligible effect on irradiation-induced hardening and embrittlement for low copper materials [10]. Thus, the difference between Materials #1 and #2 specimens reported hereafter are mainly fast neutron fluence, and to a lesser extent chemical composition. As shown in the following, combining available data for Materials #1 and #2 allows assessing both tensile properties and fracture properties for a large range of irradiation fluence and test temperature.

2.2. Tensile properties

Tensile properties have been assessed on Material #1 on flat tensile and axisymmetric notched samples machined through electro-spark erosion, at both unirradiated and irradiated states. Mechanical tests have been performed at the LECI hot cells facility (CEA Saclay). Flat tensile samples have a gage region of 25×4×2.5mm^3. Axisymmetric notched samples have a minimal diameter of 3.5mm and a notch diameter of 2.8mm. All tests have been performed under isothermal conditions between -100°C and 300°C at a mean strain rate of 5.10^{-4}s^{-1} along the gage - or notch - length. For notched samples, traction-compression tests are performed: tensile loading is applied until reaching a given level of accumulated plastic strain, then compressive loading is applied until the minimal diameter ϕ, measured by a diametral extensometer, reaches its initial value ϕ_0. Accumulated plastic strain is evaluated using the formula $p = 2\ln(\phi_0/\phi)$. Target values for the tensile loading lies between 20% and 40%. As fluence is different from one sample to the other, results are presented in the following by grouping the data. For flat tensile samples, three groups are used: Φ(E > 1MeV) = [3.6 – 4.0]10^{19}n.cm^{-2}, [5.0 – 5.4]10^{19}n.cm^{-2} and [6.8 – 7.5]10^{19}n.cm^{-2}, referred to as by their mean fluence Φ_{avg} in the following.

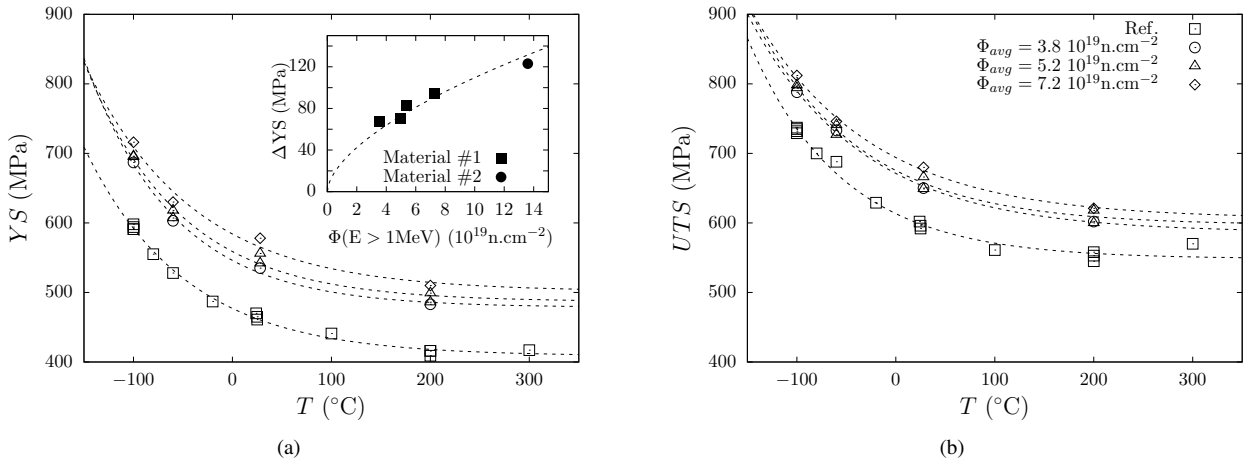

Figure 1: Conventional tensile properties (a) yield stress with a 0.2% offset YS and (b) ultimate tensile strength UTS for Material #1. Dashed lines correspond to fitting curves assuming an exponential dependence with respect to the temperature. Inset (a): Irradiation hardening ΔYS(200°C) as a function of neutron fluence for Materials #1 and #2. Dashed line corresponds to a power law fit with an exponent 0.59 [10].

Conventional tensile properties - yield stress with a 0.2% offset YS and ultimate tensile strength UTS - are shown on Fig. 1. Typical evolutions of RPV steels tensile properties are obtained with higher stresses for lower temperatures / higher fluence. At room temperature and at the unirradiated state, the Material #1 is characterized by a yield stress and ultimate tensile strength equal to 470MPa and 600MPa, respectively. A strong irradiation-induced hardening is observed: an increase of yield stress $\Delta YS = 110$MPa is observed for the maximal fluence considered $\Phi_{avg} = 7.2\ 10^{19}$n.cm^{-2}. A dynamic strain ageing is also found characterized by a non-monotonic dependence of the mechanical properties between room temperature and 300°C (Fig. 1b).

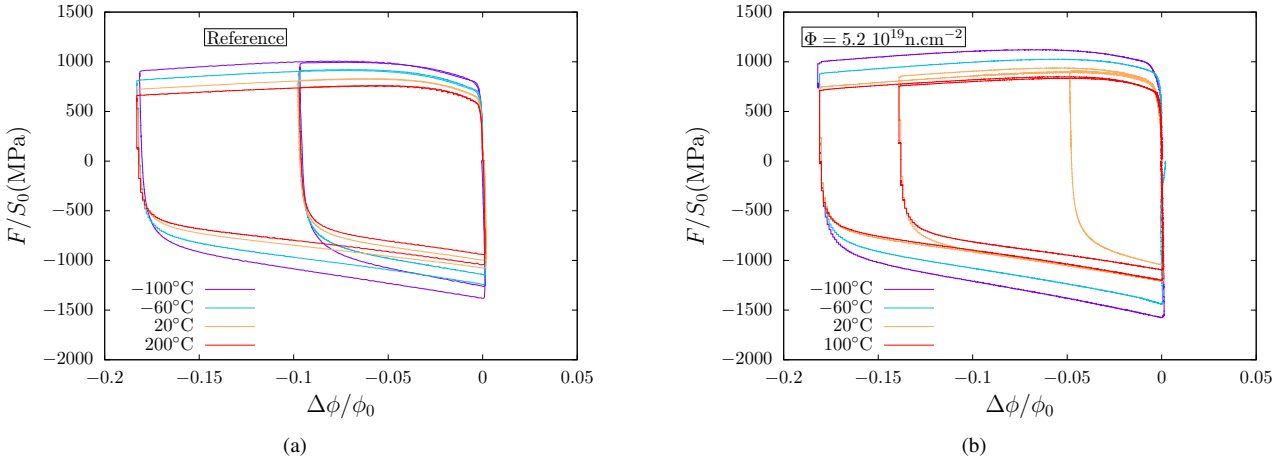

Figure 2: Conventional stress (F/S_0) as a function of the normalized diametral reduction ($\Delta\phi/\phi_0$) at the (a) unirradiated state and (b) irradiated state, for Material #1

Results for notched samples are shown in Fig. 2 for the different temperatures and fluences. At the unirradiated state (Fig. 2a), the target accumulated plastic strain is $p = 40\%$ in order to assess large strain behavior of the material. In addition, the reverse compressive loading allows evaluating the Bauschinger effect which is significant for all temperatures, where a lower yield stress in compression is observed after a tensile loading. Similar results are observed at the irradiated state (Fig. 2b) with higher stresses as fluence increases. These experimental data are consistent with the results obtained on Material #2 [42] that will be presented hereafter. Additional experimental data on notched samples are also available for other fluences (3.8 10^{19}n.cm^{-2} and 7.2 10^{19}n.cm^{-2}) and are presented in the following for the calibration of the constitutive equations.

2.3. Impact properties

Impact properties have been thoroughly characterized through Charpy V-notch test for the Material #2. In particular, for five different irradiation levels, upper shelf energy has been determined and compared to reference value obtained before irradiation [42]. Reference USE are in fact evaluated for each irradiation campaign based on specimen sampled close to the ones irradiated to account for sampling effects. In all cases, fractographic observations confirm that the fracture is ductile and related to the presence of MnS inclusions and carbides. Results are summarized in Tab. 3. First, large variation of reference USE is observed, showing that sampling effects are significant and should be accounted for to assess the evolution of USE with irradiation. More precisely, the two subsets for USE_{ref} in Tab. 3 are attributed to different orientations of the specimens: T-L and L-S for the lower and higher values, respectively. Second, a drop of USE with irradiation is systematically observed, consistently with data from the literature [18]. Note that in some cases, mostly low irradiation fluence, an increase of USE can be observed [19]. Third, the magnitude of the USE drop is affected by both the initial USE and irradiation fluence, as accounted for in ETC [9, 15, 16, 18].

Orientation	**USE_{ref}** (J)	**Fluence (E>1MeV)** (10^{19}n.cm^{-2})	**ΔUSE** (J)
L-S	222	5.2	-56
T-L	166	8.8	-27
T-L	183	11.0	-36
L-S	222	11.8	-54
T-L	170	13.7	-23

Table 3: Evolution of Upper Shelf Energy (USE) as a function of irradiation fluence for the Material #2

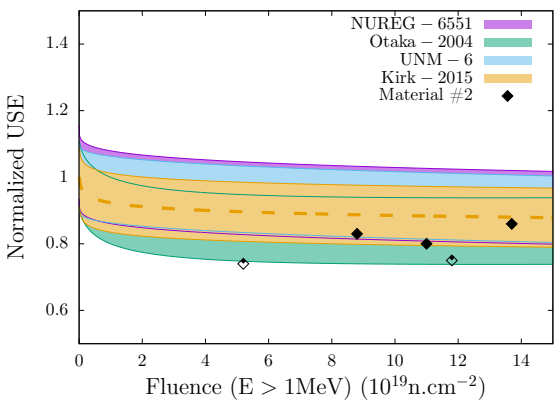

Figure 3: Evolution of the normalized USE (with respect to the reference value) as a function of irradiation fluence: Comparisons of the predictions of the models ($\pm\sigma$) to the experimental data

The experimental data are compared to the trend curves proposed in [9, 15, 16, 18] in Fig. 3. It should be noticed that all models but one (NUREG-6551) can be expressed as USE(Φ)/USE($\Phi = 0$) = $A\,\mathcal{G}(\Phi)$, where the prefactor A depends on the chemical composition and product form. For NUREG-6551, the normalized USE still depends on the reference USE. All models give consistent predictions owing to the large standard deviation associated with each model. Note also that an alternative model based on DBTT shift has been proposed in NUREG-6551 (*i.e.*, Eq. 3-6 in [9]) that leads also to prediction in agreement with these experimental results. Among the four models and for the chemical composition of Material #2, NUREG-6551 is an upper bound while Otaka-2004 is a lower bound. Experimental data from Tab. 3 are within the scatter range ($\pm\sigma$) of all models. The latest and simplest model - Kirk-2015 - shown in dashed line in Fig. 3 and defined as:

$$\mathrm{USE} = \mathrm{USE}_{\mathrm{ref}}\left[1 + L\max\left(\log_{10}\Phi(\mathrm{n.cm}^{-2}) - 17, 0\right)\right] \tag{1}$$

$$L = -\left[0.1 + 0.065\tanh\left(\frac{Cu(wt\%) - 0.18}{0.06}\right)\right] \tag{2}$$

is in rather good agreement with the experimental data, especially with the subset corresponding to the T-L orientation. Clearly, more data would be necessary for lower fluences to assess the initial decrease of USE, but are not available for the Material #2 considered. In the following, Kirk-2015 model (Eq. 1) will be used for comparisons to numerical simulations. The interesting feature of this model - compared to others - is that the only dependence to the chemical composition is the copper content, while retaining a satisfactory agreement for predicting experimental results on a large database [18]. This implies that, at least from a statistical point of view, the evolution of USE is mainly driven by irradiation-induced hardening. Irradiation might still affect other phenomenon involved in ductile fracture, *i.e.*, void nucleation or coalescence, but then Eq. 1 implies that these evolutions should be weakly dependent on chemical composition. Given that extended information are available for the material considered about the hardening behavior (Section 2.2), especially as a function of irradiation level, the main question raised in this study is the possibility to predict quantitatively the evolution of USE, removing the need for ETC such as Eq. 1. This requires modelling of the material behavior and simulating Charpy impact tests.

3. Modelling and Simulations

In this section, modelling and simulations of Charpy V-Notch tests are described with the aim of predicting USE. The modelling of the hardening behavior is first detailed for cases where ductile damage is not involved, then extended to account for porosity evolution. The finite element Charpy simulations are finally described.

3.1. Constitutive equations: Hardening behavior

Experimental data shown in Section 2.2, tensile loading on flat specimens and tension-compression tests on axisymmetric specimens correspond to cases where ductile damage can be neglected. Thus, these data can be used to calibrate the hardening behavior of the material. The constitutive equations used in the following are taken from [42]. Elasticity is described by Hooke's law, with a Young's modulus Y and a Poisson's ratio ν. Plasticity is modelled using a yield function $\mathcal{F}$ defined such as:

$$\mathcal{F} = \sigma^\star - R(p) \tag{3}$$

where $\sigma^\star$ is an equivalent stress and $R(p)$ represents the isotropic hardening. Without ductile damage, $\sigma^\star$ is computed based on von Mises equivalent stress σ_{vM} :

$$\sigma^\star = \sigma_{vM}\left(\underset{\sim}{\boldsymbol{\sigma}} - \underset{\sim}{\boldsymbol{X}}\right) \tag{4}$$

where $\sigma_{vM}(\bullet) = \sqrt{[3/2]\,\bullet' : \bullet'}$ with $\bullet' = \bullet - \mathrm{trace}\,\bullet\,\boldsymbol{I}$. $\underset{\sim}{\boldsymbol{\sigma}}$ and $\underset{\sim}{\boldsymbol{X}}$ are the Cauchy stress and a back stress to account for kinematic hardening, respectively. Viscoplastic behavior is governed by the flow rule [46]:

$$\underset{\sim}{\dot{\boldsymbol{\varepsilon}}}_p = \dot{p}\left([\mathcal{F}]_+\right)\frac{\partial \mathcal{F}}{\partial \underset{\sim}{\boldsymbol{\sigma}}} \tag{5}$$

where $[\bullet]_+$ is the positive part function. The accumulated plastic strain rate function $\dot{p}$ is defined as an harmonic sum of two Norton-like viscous laws:

$$\dot{p}(\bullet) = \left[\left(\frac{\bullet}{K_1}\right)^{-m_1} + \left(\frac{\bullet}{K_2}\right)^{-m_2}\right]^{-1} \tag{6}$$

where the parameters $\{K_1, m_1, K_2, m_2\}$ govern the viscosity of the material. Eq. 6 allows accounting for two viscous mechanisms at low and high strain rates, respectively [47]. For cases where one mechanism is almost not activated, a standard Norton viscous law is recovered. Eqs. 5, 6 lead to higher stresses as strain rate increases, which is important for the modelling of Charpy impact test where high strain rates happen close to the notch. Isotropic and kinematic hardening are defined through the evolutions of the variables R (Eq. 3) and $\underset{\sim}{\boldsymbol{X}}$ (Eq. 4), respectively. A Voce law is used for isotropic hardening:

$$R(p) = \max\left(R_0 + Q\left[1 - \exp\left(-bp\right)\right], R_l\right) \tag{7}$$

where R_l is the value of the Lüders plateau often observed in RPV steels. The kinematic hardening is ruled out by the Armstrong-Frederick law for the evolution of the back stress:

$$\dot{\underset{\sim}{\boldsymbol{X}}} = C\,\underset{\sim}{\dot{\boldsymbol{\varepsilon}}}_p - D\dot{p}\,\underset{\sim}{\boldsymbol{X}} \tag{8}$$

The hardening behavior is fully characterized by the set of parameters $\{R_0, R_I, Q, b, C, D, K_1, m_1, K_2, m_2\}$ that may depend on temperature and irradiation level. Elasticity and viscosity moduli are assumed to be independent of irradiation and are taken from previous studies [42]. The other parameters are calibrated in Section 4.1.

3.2. Constitutive equations: Ductile fracture

The set of equations presented in the previous section should be extended to account for the presence of porosity - defined as the ratio of the void volume fraction to the total volume - in order to model ductile fracture through void growth and coalescence. As shown in [48], this can be done in a seamless way by considering equivalent stresses $\sigma^\star$ other than von Mises stress in Eq. 3. In the void growth regime, the GTN model [29, 30] is used where $\sigma^\star_{gtn}$ is defined as:

$$\sigma^\star_{gtn} \quad \text{such as} \quad \left(\frac{\sigma_{vM}}{\sigma^\star_{gtn}}\right)^2 + 2q_1 f \cosh\left(\frac{3}{2}q_2\frac{\sigma_m}{\sigma^\star_{gtn}}\right) - 1 - q_1^2 f^2 \overset{\text{def.}}{=} 0 \tag{9}$$

Eq. 9 along with Eq. 3 set the stress level at which plastic flow will occur for a material of porosity f. Two limit cases can be described: for $f \to 0$, $\sigma^\star_{gtn} \to \sigma_{vM}$, the material is not porous and classical von Mises plasticity is recovered. For $f \to 1$, *i.e.*, the material is fully porous / damaged: the stress level for plastic flow tends to zero according to Eqs. 9, 3, modelling cracking. However, the GTN model is relevant for low porosity regime where voids are not interacting with each other. For high porosity, another model should be used, such as the Thomason coalescence model [49]:

$$\sigma^\star_{coa} \quad \text{such as} \quad \sigma_I \overset{\text{def.}}{=} \left[(1-\chi^2)\left(0.1\left(\frac{\chi^{-1}-1}{W}\right)^2 + 1.2\sqrt{\chi^{-1}}\right)\right]\sigma^\star_{coa} \tag{10}$$

where σ_I is the largest principal stress. W and χ are variables describing the voids: W is the void aspect ratio and χ is the void radius normalized by the distance between adjacent voids, both defined with respect to the direction of σ_I. For $\chi \to 1$, *i.e.*, voids are interconnected, Eq. 10 along with Eq. 3 imply that plastic flow will occur for $\sigma_I = 0$, again modelling cracking. Both equivalent stresses (Eqs. 9, 10) define a yield criterion (Eq. 3) associated with a plastic flow rule (Eq. 5) in order for the full model to account for both void growth and void coalescence deformation regime. Multi-surface plasticity is used: both yield criteria can be activated. In practice, except close to the transition, only one deformation mode is active at the same time: void growth for low porosity and void coalescence for large porosity. In addition, incorporating kinematic hardening (Eq. 8) in ductile fracture model is still a research topic [50]. Thus for ductile fracture simulations shown in the following, the kinematic contribution to hardening is transformed into an additional isotropic Voce hardening where the parameters of the Voce law are $\{Q, b\} = \{C/D, D\}$.

Evolution laws for the additional internal variables introduced in the previous equations - namely porosity f, normalized intervoid distance χ and void aspect ratio W - are required to have a full set of constitutive equations. The evolution of the porosity comes from mass conservation [31]:

$$\dot{f} = (1-f)\,\mathrm{trace}\,\dot{\underset{\sim}{\boldsymbol{\varepsilon}}}_p \tag{11}$$

Void nucleation can be accounted for by adding a term [36], either strain- or stress-based, in Eq. 11, but is disregarded here for simplicity. This point will be discussed later on. The parameter χ can be recovered from geometrical considerations [31]:

$$\chi = q_\chi\left(\frac{6\lambda f}{\pi W}\right)^{1/3} \qquad \dot{\lambda} = \lambda\dot{\underset{\sim}{\boldsymbol{\varepsilon}}}_I \tag{12}$$

where λ is the aspect ratio of the void distribution (assumed periodic). q_χ is a phenomenological parameter introduced to account for the effect of void distribution on coalescence phenomenon [51]. Its value is close to one and should be calibrated. The higher the value of q_χ, the higher the value of χ, the lower the coalescence stress (Eq. 10). For simplicity, void aspect ratio evolution is disregarded $\dot{W} = 0$. Finally, in order to complete the set of constitutive equations, initial internal state values are required:

$$\{f, W, \lambda\}_{t=0} = \{f_0, 1, 1\} \tag{13}$$

stating that the initial void distribution corresponds to a cubic array of spherical voids. For $\chi \to 1$ (Eq. 12) - corresponding to interconnected voids - the yield surface shrinks to a point as a result of Eq. 10, representing material failure. To avoid numerical problems close to this point, a threshold is defined $\chi_c = 0.95$ above which an additional internal variable `broken` is set to one. In that case, the output of the constitutive equations is $\underset{\sim}{\boldsymbol{\sigma}} = \underset{\sim}{\mathbf{0}}$. The constitutive equations detailed hereabove have been implemented in the `MFront` code generator [52] using an implicit integration scheme using the logarithmic framework to account for finite strains [53]. Details about this numerical implementation can be found in [54].

3.3. Charpy impact test simulations

Finite element simulations of Charpy V-Notch tests are performed using the constitutive equations described previously in the `Cast3M` finite element code [55]. The finite element meshes of the specimen, anvils and striker have been made using `Salome` platform (Fig. 4a) where quadratic reduced integration elements are used. Mesh is refined in the crack propagation area (Fig. 4b) as well as in contact areas. Frictional contact is modelled between the specimens and

the anvils / striker according to a Coulomb's law with a friction coefficient $\mu = 0.1$. Anvils and striker are assumed to be rigid. The constitutive equations used lead to mesh-dependent results [48]. A simple way to deal with such deficiency is to consider mesh size in the region where ductile crack propagates as a material parameter [36]. A fixed initial size of element *perpendicular to crack propagation* of 100μm is chosen (Fig. 4b), which is of the order of the typical microstructure relevant lengthscale [36]. Otherwise, mesh convergence has been assessed with respect to mesh density outside the crack propagation area. Due to high plastic strain rate, local heating happens close to the crack tip. Accounting for this phenomenon, as done in [36], is crucial at low temperature due to the strong evolution of mechanical properties with temperature (Fig. 1). However, this can be neglected at high temperature where mechanical properties saturate, which is done in this study.

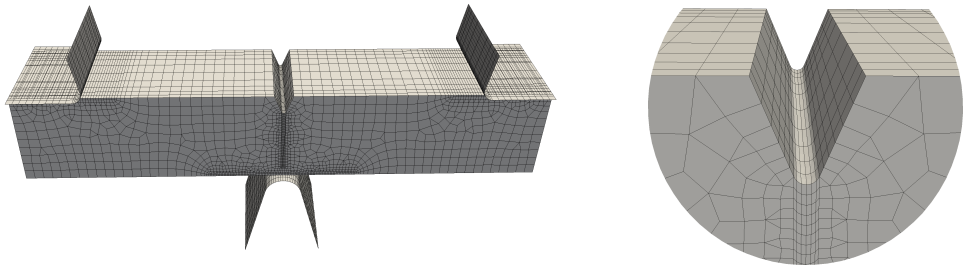

(a) (b)

Figure 4: (a) Meshes of Charpy specimen, anvils and striker. Due to symmetries, only one-fourth of the total mesh is actually used in the simulations reported hereafter. (b) Close-up view of the notch mesh.

Unless specified, simulations are performed using an initial porosity level f_0 (Eq. 13) given by the Franklin's formula [47] which considers that primary voids nucleate in RPV steels from manganese sulphur inclusions and oxides:

$$f_0 = 0.054\left(\mathrm{S}(wt\%) - \frac{0.001}{\mathrm{Mn}(wt\%)}\right) + 0.055\,\mathrm{O}(wt\%) \tag{14}$$

For Material #2 (Tab. 1), this leads to $f_0 = 4.5\,10^{-4}$, where the oxygen content has been set to O(wt%) = 0.003. To speed up numerical simulations, only one layer of elements along the crack path has a non-zero porosity. A displacement rate ot the striker of 5m.s^{-1} is applied. Quasi-static simulations are performed. Dynamical effects are thus neglected as it was shown to have a negligible effect on the overall load-displacement curves [36]. However, strain-rate effects are accounted for through the constitutive equations (Eq. 6). Two numerical strategies have been implemented and used simultaneously to increase the robustness of the simulations. First, element deletion is used based on the criterion that half of the Gauss points have the internal variable `broken` equals to one. Second, an explicit time step control strategy is used: the time step is automatically adjusted to target a maximum porosity increment $\Delta f_{target} = 3.10^{-3}$ (Eq. 11).

4. Numerical results

In this section, the parameters of the model are first calibrated based on comparisons to experimental results. Then, simulations are performed to predict the evolution of the USE with irradiation.

4.1. Calibration: Hardening behavior

Tensile tests on flat and notched specimens are used to calibrate the remaining parameters of the hardening law $\{R_0, R_l, Q, b, C, D\}$ by comparing the predictions of the model to the experimental data. For the tensile tests, uniaxial stress loading conditions are applied on a material point, while finite element simulations are performed for the notched samples. All parameters are *a priori* dependent on temperature and fluence. The hardening parameters are written as:

$$\begin{aligned} R_0(T,\Phi) &= [1+\alpha(\Phi)]r_0(T) & R_l(T,\Phi) &= [1+\alpha(\Phi)]r_l(T) \\ Q(T,\Phi) &= q(T)\exp\left[-b\beta(\Phi)\right] & C(T,\Phi) &= c(T)\exp\left[-D\beta(\Phi)\right] \end{aligned} \tag{15}$$

which says that irradiation induces both a increase of yield stress / Lüders stress and a decrease of strain hardening capability [56]. Then, following the approach proposed in [42] where a Master Curve has been determined for the tensile curves by rescaling by the flow stress:

$$\begin{aligned} q(T) &= 0.45 r_0(T) & b &= 12 \\ c(T) &= 4 r_0(T) & D &= 25 \end{aligned} \tag{16}$$

The functions $r_0(T)$ and $r_l(T)$ correspond to the flow stress and Lüders stress of the unirradiated material, and can be extracted from conventional tensile properties. Note that the slight non-monotonous dependence of flow stress between 100°C and 300°C is not modelled. The functions $\alpha(\Phi)$ and $\beta(\Phi)$ require calibration. A power-law dependence to the fast neutron fluence with an exponent 0.59 is chosen, consistently with the ETC [10]. Only the two prefactors of the functions $\alpha(\Phi)$ and $\beta(\Phi)$ remain to be calibrated, which has been done in [42] for a fluence of 12.10^{19}n.cm^{-2}. All parameters are summarized in Tab. 4.

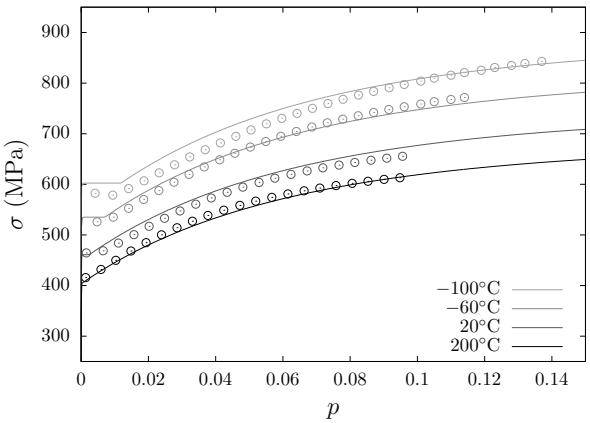

(a) Φ = 0.0 10^{19}n.cm^{-2} (E>1MeV)

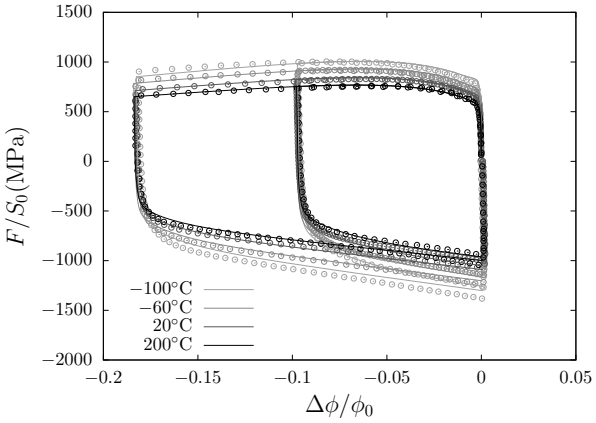

(b) Φ = 0.0 10^{19}n.cm^{-2} (E>1MeV)

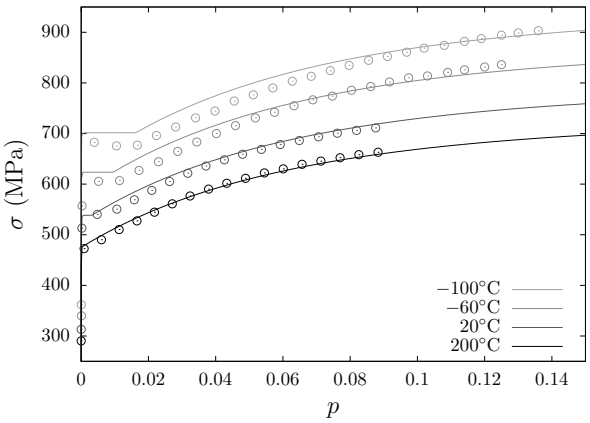

(c) Φ_{avg} = 3.8 10^{19}n.cm^{-2} (E>1MeV)

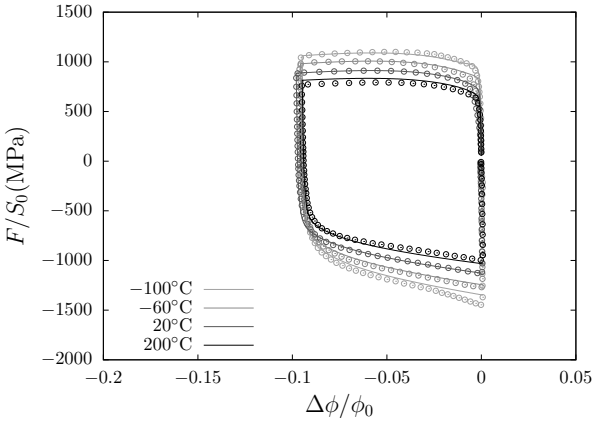

(d) Φ_{avg} = 3.8 10^{19}n.cm^{-2} (E>1MeV)

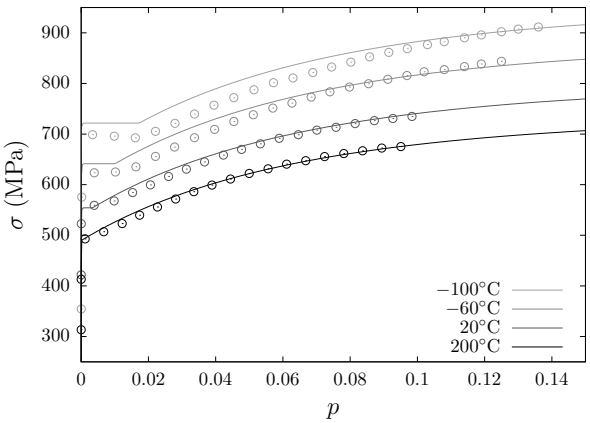

(e) Φ_{avg} = 5.2 10^{19}n.cm^{-2} (E>1MeV)

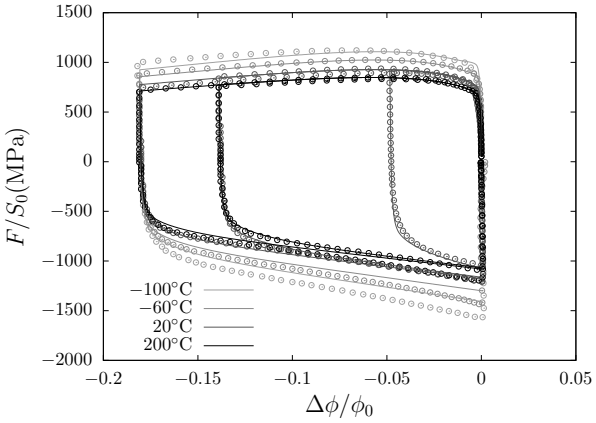

(f) Φ_{avg} = 5.2 10^{19}n.cm^{-2} (E>1MeV)

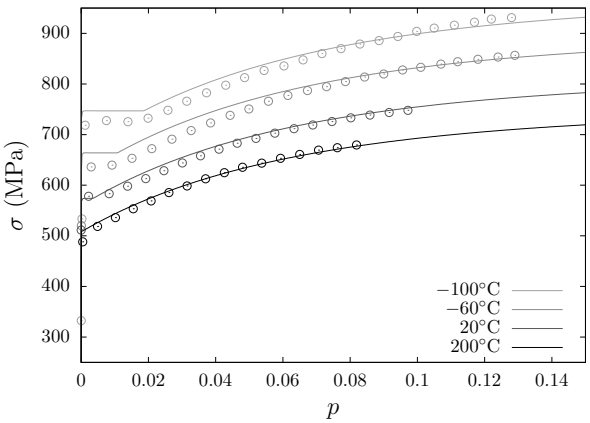

(g) Φ_{avg} = 7.2 10^{19}n.cm^{-2} (E>1MeV)

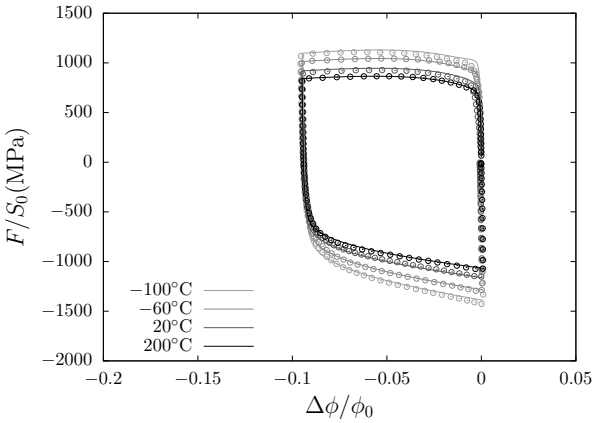

(h) Φ_{avg} = 7.2 10^{19}n.cm^{-2} (E>1MeV)

Figure 5: Comparisons between the predictions of the constitutive equations (solid lines) to the experimental data (points) for tensile tests on flat (a,c,e,g) and notched (b,d,f,h) samples, as a function of temperature and irradiation fluence, for Material #1

The comparisons between the experimental data and numerical simulations are shown in Fig. 5 for different temperatures and irradiation fluences, for Material #1. For $T \in [-100 : 200]$°C and $\Phi \in [0 : 7.2]10^{19}$n.cm^{-2}, a quantitative agreement is obtained. In particular, the hardening behavior is well captured up to strain levels of about 40% (Figs. 5b,f) under tensile loading whatever the test temperature. The Bauschinger effect, characterized by a compressive yield strength lower than tensile yield strength, is also modelled quantitatively (Figs. 5b,d,f,h) for strains levels in the range $p \in [0 : 40]$%. In some cases (Figs. 5f), slight deviations are observed under compressive loading after tensile loading, indicating some limitations of the constitutive equations calibrated for cases involving low temperature / high strain levels and reverse loading. This case is however not relevant for the simulations presented hereafter in this study.

		Material #1	Material #2
Y	(MPa)	$197600 - 118.8T(°C)$	
ν		0.3	
r_0	(MPa)	$400 + 33\exp(-0.011T(°C))$	$430 + 10\exp(-0.019T(°C))$
r_l	(MPa)	$400 + 48\exp(-0.012T(°C))$	$461 + 28\exp(-0.016T(°C))$
q	(MPa)	$0.45r_0$	
b		12	
c	(MPa)	$4r_0$	
D		25	
K_1		$80 - 0.5\min[T(°C), 20]$	
m_1		7	
K_2		0.185	
m_2		1.15	
α		$0.35\left(\frac{\Phi(10^{19}\text{n.cm}^{-2})}{12}\right)^{0.59}$	
β		$0.012\left(\frac{\Phi(10^{19}\text{n.cm}^{-2})}{12}\right)^{0.59}$	

Table 4: Parameters of the constitutive equations: Hardening parameters

The hardening parameters have been calibrated based on Material #1, but Charpy tests simulations should be performed on Material #2 to compare with the experimental data. Differences of chemical composition are rather minor (Tab 1), but an additional calibration is required regarding the flow stress and Lüders stress values at the unirradiated state. This has been done in [42] and calibrated values are given in Tab. 4. Comparisons between experimental data and numerical simulations for notched tensile samples are shown in Fig. 6 for different temperatures and irradiation fluences. As for Material #1, a very good agreement is obtained regarding the hardening behavior up to high strain levels. It should be kept in mind that only flow stress and Lüders stress values at the unirradiated state differ between Material #1 and Material #2, all other parameters being either fixed or related to these values (Tab. 4).

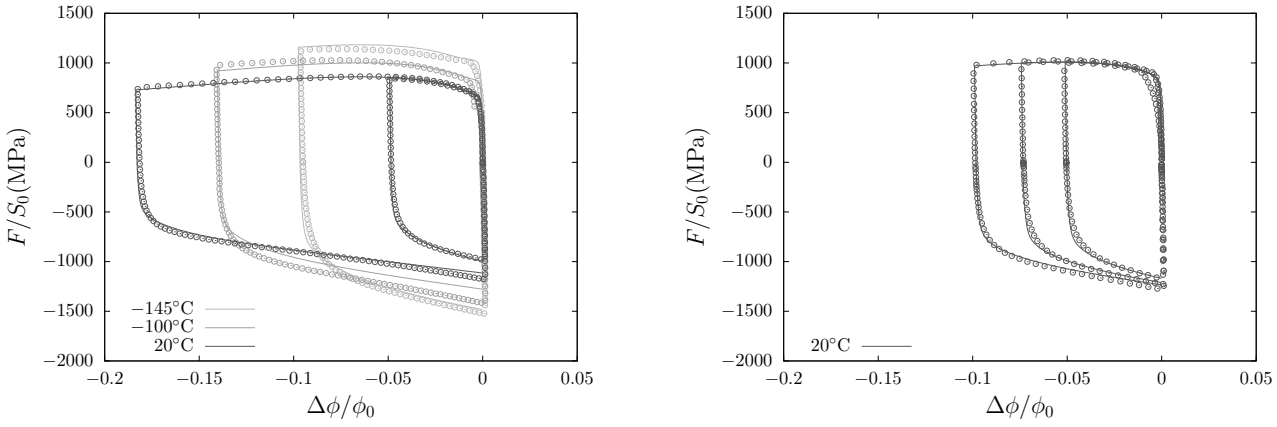

(a) Φ = 0.0 10^{19}n.cm^{-2} (E>1MeV) (b) Φ = 10.0 10^{19}n.cm^{-2} (E>1MeV)

Figure 6: Comparisons between the predictions of the constitutive equations (solid lines) to the experimental data (points) for tensile tests on notched samples, as a function of temperature and irradiation fluence, for Material #2

The experimental database obtained in this study allows calibrating the hardening behavior of the material for a wide range of parameters (temperature, fluence, strain), covering the whole range of relevant applications for RPV. This includes quasi-static and dynamic structural integrity assessment between room temperature to operating temperature up to fluence relevant for long-term operation of PWR reactors [6] or analysis of low temperature laboratory tests assessing fracture toughness evolution with irradiation [42]. The key point is the parameterization of the hardening variables where the temperature dependence is supported only by the unirradiated flow stress r_0 and the irradiation dependence only by two hardening variables α and β. This allows accounting for material variations of the unirradiated material through

changing only the flow stress, as shown hereabove between Material #1 and Material #2. A simple dependence of the parameters α and β to neutron fluence is used that appear to be sufficient for the (low Cu content) materials considered in this study. However, more complicated functions may be required. More generally, an interesting perspective is to validate such modelling assumption for a large database of RPV steels. The prefactors of the irradiation hardening variables are assumed to depend on the chemical composition. This quantitative modelling of hardening behavior of RPV steels allows going beyond the hypothesis made for example in [39] in order to predict quantitatively the Charpy impact properties. Before, ductile fracture model parameters should also be calibrated, which is done in the next section.

4.2. Calibration: Ductile fracture

Accounting for porosity through Eqs. 9, 10 requires to calibrate some parameters. In the GTN model (Eq. 9), the parameters are q_1 and q_2 that have been shown in previous studies to depend on strain-hardening, void distribution, stress triaxiality. Preliminary simulations using the tabulated values including the effect of strain hardening given in [57] show a rather minor effect. Thus, in the following, these parameters are set to the values most commonly used in the literature: $q_1 = 1.5$ and $q_2 = 1$. In the coalescence model used, the only parameter is q_χ (Eq. 12). This parameter should be viewed as an effective parameter describing void distribution. For a cubic array of spherical voids, the theoretical value is $q_\chi = 1$ [51]. Here, q_χ is calibrated based on Charpy V-Notch simulations. Experimental Charpy load-displacement curves available for Material #2 for three conditions on the upper shelf - $\{\Phi = 0.10^{19}\text{n.cm}^{-2}, T = 300°\text{C}\}$, $\{\Phi = 8.8\,10^{19}\text{n.cm}^{-2}, T = 150°\text{C}\}$ and $\{\Phi = 13.7\,10^{19}\text{n.cm}^{-2}, T = 235°\text{C}\}$ - are compared to the numerical curves, and the parameter q_χ is adjusted. Note that only data corresponding to the T-L orientation are used (see Section 2.3) for which the strain-hardening behavior has been calibrated.

Fig. 7a corresponds to the typical output of Charpy finite element simulations, where plastic strain p field is shown on the deformed configuration for an extended crack propagation. Several features can be observed. First, for Charpy impact tests in the upper shelf range, a significant amount of plasticity is observed at the contact between the specimens and the anvils / striker. This may induce numerical difficulties for the frictional contact algorithm. It should also be noted that accounting for friction, although with a moderate value of the coefficient $\mu = 0.1$, leads to runtimes about twice the ones using frictionless contact. Friction leads to an increase of the load of about 3% compared to frictionless contact. Along the crack propagation path, plastic strain is higher close to the initial notch where crack nucleates. As discussed in Section 3.3, simulations are mesh-dependent, hence plastic strain values depend on mesh size.

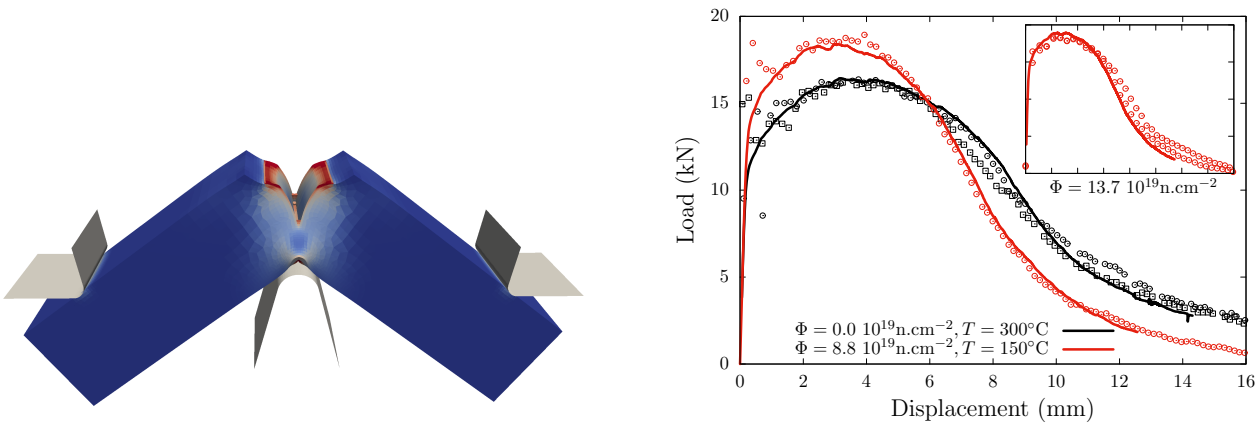

(a) (b)

Figure 7: (a) Typical plastic strain field of the finite element Charpy simulations (b) Load-displacements curves for Material #2: solid lines correspond to numerical results and points to experimental data

For unirradiated and irradiated states, several values of the coalescence parameter q_χ have been tested to obtain the best agreement between numerical and experimental load-displacement curves (Fig. 7b). At the unirradiated state, a value of $q_\chi = 0.9$ is obtained, while a higher value - $q_\chi = 0.975$ - is required at the irradiated state ($\Phi = 8.8\,10^{19}\text{n.cm}^{-2}$). As shown in Fig. 7b, a very good agreement is observed between numerical predictions and experimental data for the whole curves, *i.e.*, up to almost complete fracture of the specimens. Note that simulations are stopped when the load is about 20% of the maximal load, as convergence is extremely difficult when only few elements are left in the remaining ligament (Fig. 7a). The need to change the ductile fracture parameters with irradiation seems to indicate that irradiation affects not only strain-hardening behavior but also local fracture properties. This is in agreement with the preliminary observations from [39] where the change of hardening behavior with irradiation was deemed insufficient to lead to evolutions of USE. The change of the parameter q_χ is rather small, about 10% between unirradiated and highly irradiated state, but unavoidable to predict quantitatively load-displacement curves. From a physical point of view, irradiation may affect the three different stages of ductile fracture, *i.e.*, nucleation, growth and coalescence. For simplicity, void nucleation has been disregarded in the model used, contrary to [36]. Adding the nucleation model proposed in [36] do affect slightly the load-displacement curves shown on Fig. 7b as detailed in Appendix A. However, void nucleation could also affect indirectly void growth and coalescence through the parameters q_1, q_2, q_χ by changing microscopic scale hardening behavior. Typically, void nucleation from carbides (below $1\mu m$) in between voids nucleated from MnS inclusions (above few μm) is expected

to favor void coalescence, as shown in [58]. This may provide a rationale for the evolution of the parameter q_χ with irradiation, but experimental data are required to support this hypothesis. In practice, an evolution law for the parameter q_χ as a function of irradiation is needed. The database of this study (Fig. 3) for Material #2 lacks data at low fluence. Thus a simple power-law is chosen:

$$q_\chi = 0.9 + 0.075\left(\frac{\Phi(10^{19}\text{n.cm}^{-2})}{9}\right)^{0.59} \tag{17}$$

where the exponent is taken to be equal as the one describing irradiation hardening. This is clearly an assumption that should be validated specifically, for example by performing the calibration shown on Fig. 7b for low irradiation fluence. As shown on the inset of Fig. 7b, Eq. 17 leads to accurate results for the highest fluence that was not used to calibrate the parameter q_χ.

4.3. Effect of irradiation on the upper shelf energy

The calibrated set of constitutive equations describing the ductile regime of RPV steels is used to predict numerically the effect of irradiation of the upper shelf energy. Simulations are performed at a temperature of 300°C, thus corresponding to the upper shelf, for various fluences up to 14.10^{19}n.cm^{-2}.

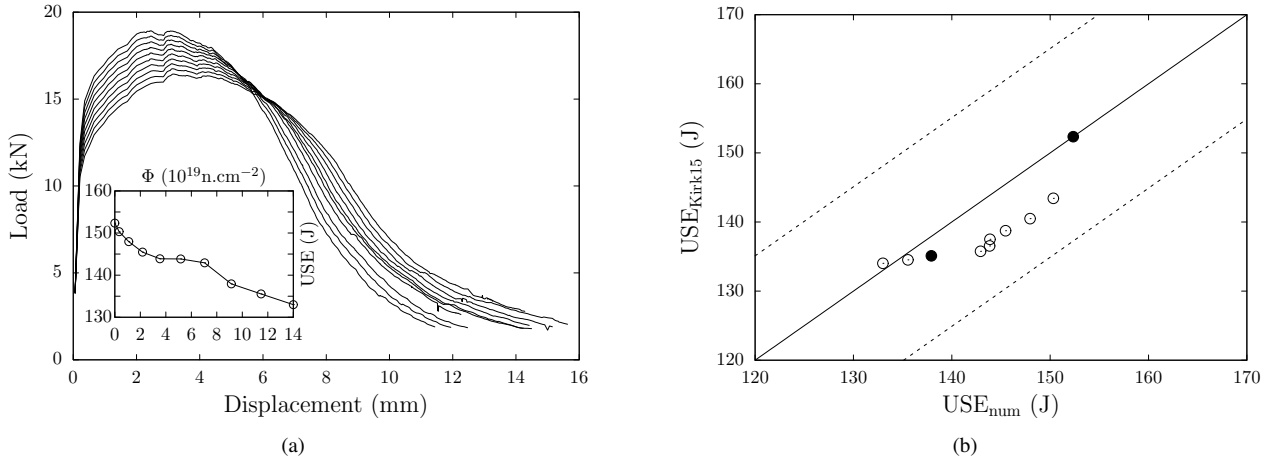

Figure 8: (a) Evolution of Charpy impact test load-displacement curves for Material #2 at a temperature of 300°C for various fluences up to 14.10^{19}n.cm^{-2}. Inset: Evolution of USE as a function of irradiation fluence. (b) Comparison of the USE estimated numerically as a function of the USE predicted by the Kirk-2015 model. Black points correspond to fluences at which calibration was performed. Dashed lines correspond to $\pm\sigma$.

Load-displacement curves are shown in Fig. 8a. Simulations are stopped when the load falls below 20% of the maximal load, as severely distorted finite elements and contact issues make convergence of the algorithm difficult. The associated fracture energy is obtained by integrating the load-displacement curves. Although not considering the final part of the curves (below 20% of the maximal force), this methodology leads to values within 3% of the fracture energy measured experimentally for the curves shown on Fig. 7b. Hence, in the following, these values are referred to as USE. Results are shown in the inset of Fig. 8a. The decrease of the USE with irradiation is recovered, about 15% for the maximal fluence considered, which is in agreement with the experimental data (Fig. 3). The values obtained numerically are compared to the predictions of the Kirk-2015 model (Eq. 1) in Fig. 8b. Reminding first that ductile fracture model parameter has been calibrated for fluences of 0 and 8.8 10^{19}n.cm^{-2} and second that the Kirk-2015 model describes the experimental data rather accurately (Fig. 3), this explains that the two points in black in Fig. 8b shows an almost perfect agreement. The interesting point is that the evolution in between predicted numerically follows quite closely the Kirk-2015 model, and the differences are well below the scatter of the latter. This indicates that assuming a power-law dependence of the ductile fracture parameter (Eq. 17) with an exponent equal to the one used for irradiation hardening is relevant, at least at first order. In more details, the data shown on Fig. 8b suggests that the exponent should be lower than 0.59, *i.e.*, a stronger decrease of the parameter q_χ for low irradiation fluence, to recover the Kirk-2015 trend curve.

In this section, it has been demonstrated that the effect of irradiation on RPV Charpy impact tests load-displacement curves can be modelled quantitatively. This involves the calibration of a single parameter related to void coalescence. The range of variations of this parameter with irradiation is rather narrow, about 10% between the reference state to $\Phi = 10^{20}$n.cm^{-2}, but necessary to predict a decrease of USE with irradiation as observed experimentally. This confirms the suggestion made in [39] that accounting solely for the evolution of hardening is not sufficient. The evolution of USE with irradiation obtained numerically is consistent with the predictions from ETC such as the Kirk-2015 model. This has been done for one set of material parameters (Material #2) and for the constitutive equations described in Section 3. In the next section, other material parameters are considered as well as a simplified ductile fracture model.

5. Discussion

5.1. Effect of material parameters

Results presented in Section 4.3 indicate that, for a given material, quantitative modelling of strain-hardening and calibration of a single parameter related to ductile fracture allow to recover the evolution of the USE with irradiation. In this section, numerical experiments are performed to assess if such conclusion holds for other material parameters. More precisely, the main question concerns the relevance of Eq. 17 for other material parameters. As discussed in Section 2.3, the Kirk-2015 (Eq. 1) suggests that the evolution of ductile fracture parameters may not depend strongly on the chemical composition, as alloying elements susceptible to affect for example void nucleation (like *P* segregating at interfaces) does not appear in the model. Moreover, contrary to the NUREG-6551 model, the reference USE appears simply as a scaling factor in the Kirk-2015 model. Therefore, two numerical tests are done. The first test consists of changing the initial porosity while keeping the same hardening and fracture parameters. An initial porosity of $f_0 = 9\,10^{-4}$ is used, twice the one used in Section 4.3. The second test consists of considering a material with twice as copper as Materials #1 & #2 as this element is known to affect the evolution of USE with irradiation [9, 15, 16, 18]. As copper content affects irradiation-induced hardening, the parameters α and β of the strain-hardening behavior are modified in the following way:

$$\delta_{\alpha,\beta} = \frac{\alpha(\%Cu_2)}{\alpha(\%Cu_1)} = \frac{\beta(\%Cu_2)}{\beta(\%Cu_1)} = \frac{\Delta YS(\%Cu_2)}{\Delta YS(\%Cu_1)} = \frac{\Delta T_{FIM}(\%Cu_2)}{\Delta T_{FIM}(\%Cu_1)} \tag{18}$$

where the increase of yield stress ΔYS is assumed to be proportional to the shift of ductile-brittle transition temperature ΔT [12]. ΔT is computed with the FIM model [10] that depends on the chemical composition, leading to $\delta_{\alpha,\beta} = 1.43$ for a twofold increase of the copper content for Material #2, *i.e.*, wt% Cu = 0.14. Other material parameters are kept constant.

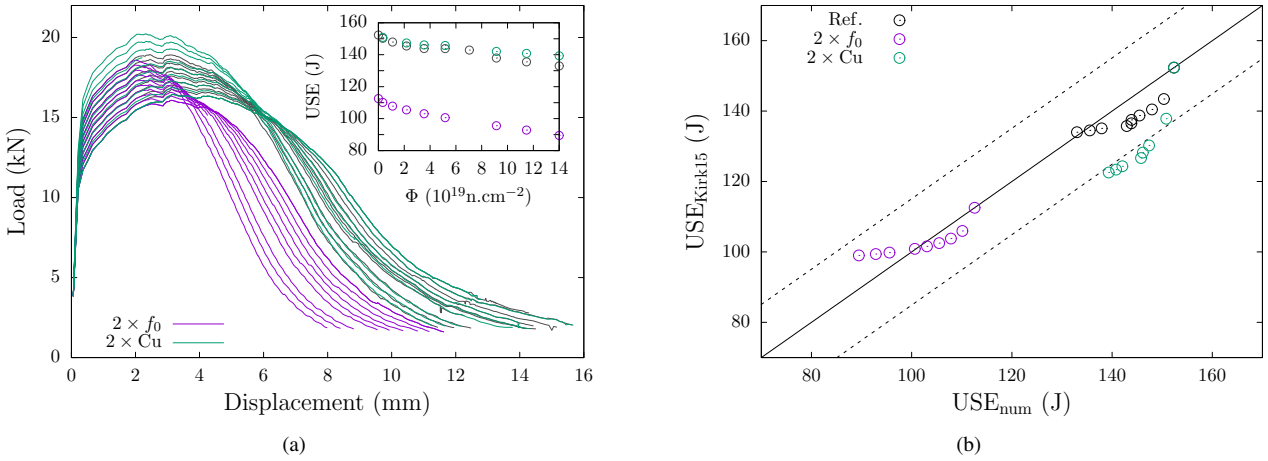

(a) (b)

Figure 9: (a) Evolution of Charpy impact test load-displacement curves at a temperature of 300°C for various fluences up to 14.10^{19}n.cm^{-2} by considering different initial porosity and copper content from Material #2. Grayscale lines correspond to the reference results from Fig. 8. Inset: Evolution of USE as a function of irradiation fluence. (b) Comparison of the USE estimated numerically as a function of the USE predicted by the Kirk-2015 model. Dashed lines correspond to $\pm\sigma$.

Results for the two tests are shown in Fig. 9 along with the reference results of Material #2 already shown in Fig. 8. For the higher initial porosity, a strong effect is as expected observed on the load-displacement curves (Fig. 9a), leading to a USE at the unirradiated state significantly lower that the reference case. The decrease of USE with irradiation follows closely the Kirk-2015 model (Fig. 9b). For the higher copper content, the effect is a higher maximal load as irradiation increases, consistently with the higher irradiation-induced hardening (Eq. 18). However, the softening part of the load-displacement curve is weakly affected. These two effects lead to a slightly higher USE at the irradiated state compared to the reference case (Inset Fig. 9a). Kirk-2015 predicts a stronger evolution of the USE (Fig. 9b), but numerical values fall within the scatter bounds of the model. Considering that the Kirk-2015 model as the reference, these two numerical tests suggest that Eq. 17 might also be relevant for a large class of RPV steels. Direct comparisons to experimental data are nevertheless required to assess this assumption in more details.

5.2. Effect of ductile fracture model

The ductile fracture model detailed in Section 3.2 combines two physically-based model to describe void growth and coalescence regimes. Another formulation, widely used in the literature, is to consider only the GTN definition of the equivalent stress (Eq. 9) with an effective porosity $f^\star$ defined as:

$$f^\star = \begin{cases} f & \text{for } f \leq f_c \\ f_c + \delta(f - f_c) & \text{otherwise} \end{cases} \quad \text{with} \quad \delta = \frac{q_1^{-1} - f_c}{f_R - f_c} \tag{19}$$

to account for coalescence in a phenomenological way as an increase of the porosity rate. Two parameters are involved: the critical porosity f_c and the fracture porosity f_R that require calibration. Eqs. 9, 19 define the full GTN model which is available in the constitutive equations library of the `MFront` code generator [54]. Following the methodology used

in Section 4, the parameters f_c and f_R are calibrated by comparing the numerical predictions to the experimental load-displacement curves. Details are given in Appendix A, leading to:

$$f_R = 0.47 - 0.06\left(\frac{\Phi(10^{19}\text{n.cm}^{-2})}{9}\right)^{0.59} \tag{20}$$

$$f_c = 0.003 \tag{21}$$

where a power-law function is again assumed for the evolution of the parameter f_R with irradiation. Numerical and experimental load-displacement curves are shown in Fig. 10a for Material #2, where a good agreement is observed. As for the other ductile fracture model, the agreement comes at the price of modifying the parameter related to void coalescence towards a stronger coalescence phase after irradiation. The model calibrated is then used to assess the evolution of the USE with irradiation for Material #2 as well as considering a higher initial porosity.

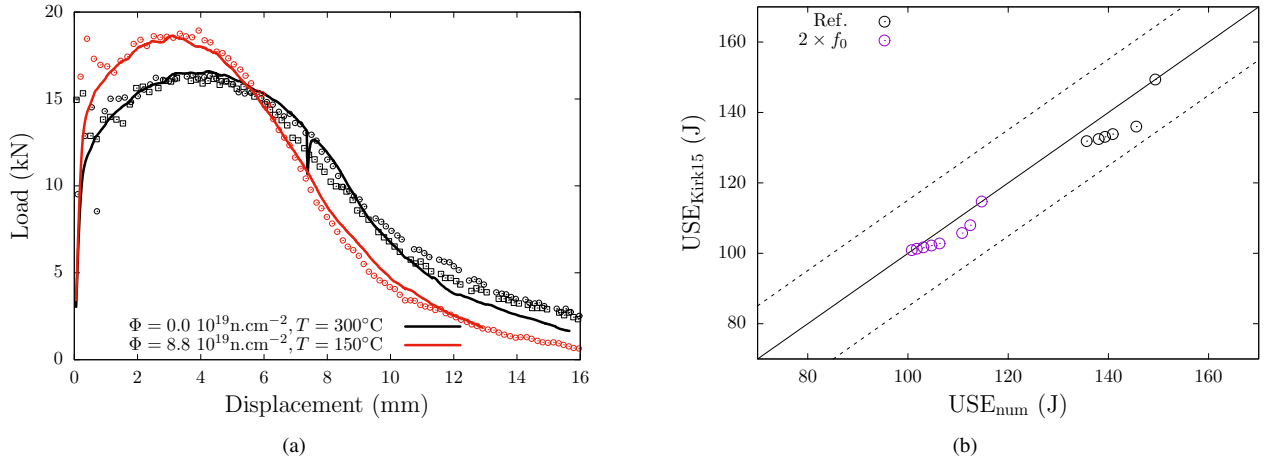

Figure 10: (a) Load-displacement curves for Material #2: solid lines correspond to numerical results (GTN model) and points to experimental data (b) Comparison of the USE estimated numerically as a function of the USE predicted by the Kirk-2015 model. Dashed lines correspond to $\pm\sigma$.

Fig. 10b shows the comparison of the USE predicted by the numerical simulations to the values predicted by the Kirk-2015 model. The results are similar to the ones presented in Section 4.3, showing that the evolution laws for the ductile fracture parameters (Eq. 20) lead to results compatible with the Kirk-2015 model.

5.3. Towards a simulation-based USE curve

The results obtained in this study indicate that the evolution of USE with irradiation for a given RPV steel can be reproduced quantitatively using direct simulations of Charpy impact tests. However this requires (1) an accurate description of the hardening behavior but also (2) calibration of fracture parameters. These requirements may be seen at first view as strong constraints to extend these results to other RPV steels, but the following approach could be used.

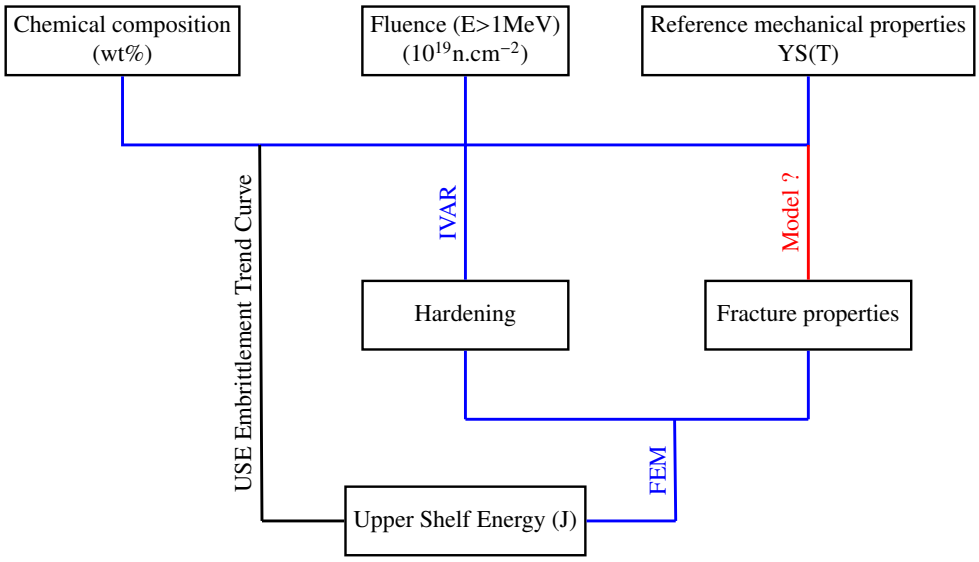

Figure 11: Flowchart for the prediction of the Upper Shelf Energy for RPV steels

First, as shown in this study for the two materials and a large range of temperature, a master curve for hardening behavior could be derived for wide class of RPV steels, reducing the need for calibration of the unirradiated material to a

single parameter, the flow stress R_0, that can be taken equal to the yield stress YS. Second, the evolution of the flow stress with irradiation is well documented in the literature for a wide range of chemical composition, *e.g.* in the IVAR data, and can be used to get the hardening parameters α and β as done in the previous section. Third, the initial porosity can be evaluated using Franklin's formula based on the chemical composition. The trickiest point is related to the calibration of the ductile fracture parameters (q_χ for the model used in Section 4, f_c and f_R for the GTN model). One of the main result of this study is that constant ductile fracture parameters does not lead to the correct evolution of USE with irradiation. Thus, a dependence to irradiation fluence has to be accounted for. Such dependence is rather weak but unavoidable, with the models used, to get predictions in quantitative agreement with experimental data. Two strategies may be proposed to obtain these parameters. The first one involves detailed assessment of local ductile fracture properties with irradiation through metallurgical and fracture surface observations. The second one consists of using the large database available for RPV steels to propose laws for ductile fracture parameters and to assess the dependence to the chemical composition. In the latter approach, the fact that the correlation proposed by Kirk depends only on the copper content, which affects only irradiation-induced hardening, suggests that the evolution proposed (Eqs. 17, 20) might be sufficient for a large class of RPV steels. Numerical tests performed in Section 5 support this assumption that remains to be fully assessed. The flowchart shown in Fig. 11 summarizes the different ways to evaluate the upper shelf energy of RPV steels, *i.e.*, based on trend curves or relying on numerical simulations. For the latter, the blue lines correspond to links that are rather mature in the literature, such as the estimation of hardening based of chemical composition and fast neutron fluence, and the numerical evaluation of USE based on finite element simulations. The main contribution of this study is towards the link that appear as a red line, where a dependence to irradiation level has been put forward.

6. Conclusions and Perspectives

Numerical predictions of the effect of irradiation on the Charpy Upper Shelf Energy of Reactor Pressure Vessel steels have been presented in this study. These predictions are based on finite element simulations of Charpy impact test based on physically-based constitutive equations modelling ductile fracture through void growth to coalescence. The parameters of the constitutive equations related to strain-hardening and fracture have been calibrated based on an experimental database for a A508 Cl3 steel. The main results of this study are the following. First, accounting only for the evolution of (strain)-hardening with irradiation does not allow to recover the decrease of USE with irradiation observed experimentally. This numerical observation is obtained for two different ductile fracture models, strongly suggesting that irradiation has an effect on local fracture features. For the material considered, calibration of the ductile fracture model parameters has been performed at both unirradiated and highly irradiated states, allowing to recover the decrease of USE. A simple power-law dependence of the ductile fracture parameter with irradiation is shown to lead to evolutions consistent with the embrittlement trend curves proposed in the literature, for different initial material parameters. ETC suggests that the evolution of USE is mostly related to the copper content - and only to this in Kirk-2015 model - hence not to chemical elements supposed to affect directly ductile fracture mechanisms such as Phosphorus weakening interfaces. Thus, the evolutions of ductile fracture parameters obtained in this study are assumed to be weakly dependent on the chemical composition of the material, therefore applicable to a wide class of RPV steels. This leads to a numerical methodology that can be used to predict USE for irradiated RPV. This methodology does not aim to replace ETC for engineering applications, but rather to build a consistent modelling of ductile fracture relevant for a wide class of RPV steels, able to predict not only USE but also fracture toughness.

Three main perspectives can be proposed based on the results obtained in this study. First, modelling and numerical simulations should be improved to be able to reproduce features that can be measured experimentally such as lateral contraction and the occurrence of shear lips on Charpy specimens. Second, additional experimental characterization are required to support the evolution of ductile fracture parameters with irradiation. This may include detailed characterization of fracture surfaces and / or X-ray tomography experiments to assess the effect of irradiation on void nucleation and / or void coalescence. Such characterization may also give some insights into the typical fracture lengthscale - set by the size of the finite element in this study - and its dependence to porosity. Thirdly, for the material considered, the database of USE values at the irradiated state was restricted to rather large neutron fluences, while the decrease of USE is stronger for low neutron fluences. Hence, the accurate calibration of the power-law dependence of the ductile fracture parameter was not possible. Numerical assessment of extended database is thus expected to lead on the one hand to refined calibration of the evolution of ductile fracture parameters with irradiation, and on the other hand to the assessment of the dependence to the chemical composition and the state of the material prior to irradiation.

Acknowledgements

The authors thank B. Courtois for the material supply, P. Grange and J. Pegaitaz for performing the tensile tests, A. Courcelle and B. Tanguy for fruitful discussions. Support from LIDEC and LECI hot cells staff is also greatly acknowledged. This study has been performed within the frame of a collaborative project between CEA and EDF.

Appendix A

Void nucleation has been considered in [39] for a RPV steel by modifying the equation related to the evolution of the porosity according to:

$$\dot{f} = (1 - f)\,\mathrm{trace}\,\dot{\boldsymbol{\varepsilon}}_p + A_n \dot{p} \tag{22}$$

where $A_n = 0.038$ for $p \in [0.5 : 1.1]$ to model void nucleation from carbides. In this study, void nucleation has been neglected. Fig. 12a shows the effect of accounting for void nucleation on Charpy load-displacement curves, using the parameter q_χ calibrated as a function of fluence. The effect is rather slight. One may however note that the effect of increasing nucleation rate is qualitatively similar to increasing the value of the parameter q_χ. The inset of Fig. 12a shows the curves obtained considering the unirradiated value of q_χ, without or with nucleation. The numerical predictions are not in quantitative agreement with the experimental curve, but increasing the nucleation rate may lead to a good agreement. Whatever the modelling chosen (effective parameter q_χ or accounting explicitly for nucleation through A_n), two key questions remain: (1) what is the most relevant fracture mechanism related to void nucleation from carbides: increasing porosity *vs.* accelerated coalescence of larger scale voids, (2) in any cases, how to calibrate these parameters and to corroborate with fractographic observations.

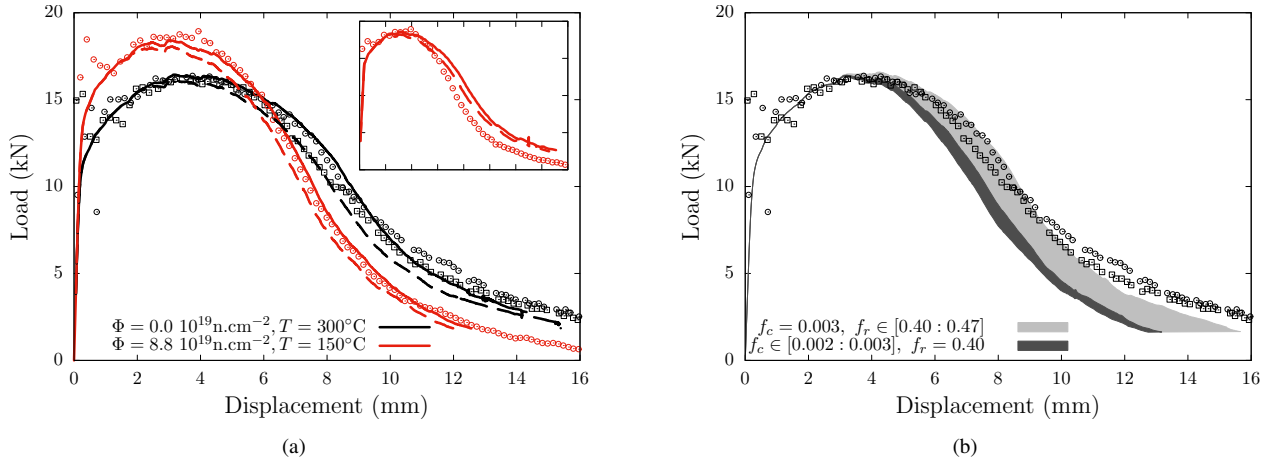

Figure 12: (a) Load-displacement curves for Material #2: solid lines and dashed lines correspond to numerical results using Eq. 17 without and with void nucleation (Eq. 22), respectively, and points to experimental data. Inset: $q_\chi = 0.9$ (b) Calibration of the GTN model: effect of the parameters f_c and f_R on load-displacement curves and comparison to experimental data

Fig. 12b shows the calibration process of the GTN model parameters (Section 5.2) at the unirradiated state where shaded areas correspond to the regions spanned by the numerical curves by varying one parameter at a time. In that case, the numerical curves are much more sensitive to the parameter f_R than f_c. Hence, the latter one has been set to $f_c = 0.003$ (by keeping the same ratio f_0/f_c as in [39]), and a good agreement is obtained for $f_R = 0.47$.

References

[1] C. English, J. Hyde, 3.03 - Radiation damage of reactor pressure vessel steels, in: R. J. Konings, R. E. Stoller (Eds.), Comprehensive Nuclear Materials (Second Edition), Elsevier, Oxford, 2012, pp. 169–196.

[2] T. Planman, W. Server, M. Yamamoto, 3.04 - Fracture toughness master curve of bcc steels, in: R. J. Konings, R. E. Stoller (Eds.), Comprehensive Nuclear Materials (Second Edition), Elsevier, Oxford, 2020, pp. 197–225.

[3] D. Curry, Cleavage micromechanisms of crack extension in steels, Metal Science 14 (1980) 78.

[4] K. E. Puttick, Ductile fracture in metals, Phil. Mag. 4 (1959) 964–969.

[5] W. L. Server, The bases for LWR vessel surveillance programs in the USA, in: W. Server, M. Brumovsky (Eds.), International Review of Nuclear Reactor Pressure Vessel Surveillance Programs, ASTM International, West Conshohocken, PA, 2018, pp. 1–8.

[6] P. Todeschini, L. Pineau, B. Courtois, Y. Shen, M. Gharbaoui, N. Jardin, Experience gained in reactor pressure vessel surveillance programs in france, in: W. Server, M. Brumovsky (Eds.), International Review of Nuclear Reactor Pressure Vessel Surveillance Programs, ASTM International, West Conshohocken, PA, 2018, pp. 184–201.

[7] E1921, Standard test method for determination of reference temperature T_0 for ferritic steels in the transition range, ASTM.

[8] IAEA, Master curve approach to monitor fracture toughness of reactor pressure vessels in nuclear power plants, Tech. Rep. IAEA-TECDOC-1631, International Atomic Energy Agency (2009).

[9] E. Eason, J. Wright, G. Odette, Improved embrittlement correlations for reactor pressure vessel steels, Report NUREG/CR-6551, U.S. Nuclear Regulatory Commission (1998).

[10] P. Todeschini, Y. Lefebvre, H. Churier-Bossennec, N. Rupa, G. Chas, C. Benhamou, Revision of the irradiation embrittlement correlation used for the EDF RPV fleet, in: Proceedings of Fontevraud 7 Contribution of Materials Investigations and Operating Experience to LWRs' Safety, Performance and Reliability, 2010.

[11] Y. Hashimoto, A. Nomoto, M. Kirk, K. Nishida, Development of new embrittlement trend curve based on japanese surveillance and atom probe tomography data, Journal of Nuclear Materials 553 (2021) 153007.

[12] E. Eason, G. Odette, R. Nandstad, T. Yamamoto, A physically based correlation of irradiation-induced transition temperature shifts for RPV steels, Report, U.S. Nuclear Regulatory Commission (2007).

[13] G. Odette, T. Yamamoto, T. Williams, R. Nanstad, C. English, On the history and status of reactor pressure vessel steel ductile to brittle transition temperature shift prediction models, Journal of Nuclear Materials 526 (2019) 151863.

[14] K. Sakamoto, S. Hatano, Development of evaluation method on integrity of RPV at the upper shelf region, Pressure Vessels and Piping Conference, 2002, pp. 11–16.

[15] M. Otaka, T. Osaki, Reduction of upper shelf energy of highly irradiated RPV steels, in: 30^{th} MPA-seminar in conjunction with the 9^{th} German-Japanese seminar, 2004.
[16] M. Kirk, A new relationship for upper shelf energy drop, in: IAEA specialists' meeting on irradiation embrittllement, 2010.
[17] M. Kirk, M. Yamamoto, M. Erickson, Assessment of the Continued Need for Independent Requirements on Transition Temperature and Upper Shelf Charpy Impact Toughness Metrics in Regulations Pertaining to Nuclear Reactor Pressure Vessels, Vol. Volume 1: Codes and Standards of Pressure Vessels and Piping Conference, 2020.
[18] M. Gordon, M. Kirk, Development of a trend curve for Charpy Upper Shelf Energy (USE) drop using USA surveillance data, in: International workshop on RPV embrittlement and surveillance programs, 2015.
[19] R. Gérard, W. De Koster, R. Chaouadi, D. Bertois, D. Martens, Irradiation effects on upper shelft energy and J-R curves of belgian RPV steels, in: Proceedings of Fontevraud 9 Contribution of Materials Investigations and Operating Experience to LWRs' Safety, Performance and Reliability, 2018.
[20] Y. Nishiyama, M. Yamaguchi, K. Onizawa, A. Iwase, H. Matsuzawa, Irradiation-induced grain-boundary solute segregation and its effect on ductile-to-brittle transition temperature in reactor pressure vessel steels, ASTM Special Technical Publication 1513 STP (2010) 153–163.
[21] E. Kuleshova, B. Gurovich, Z. Bukina, A. Frolov, D. Maltsev, E. Krikun, D. Zhurko, G. Zhuchkov, Mechanisms of radiation embrittlement of VVER-1000 RPV steel at irradiation temperatures of (50 − 400)°C, Journal of Nuclear Materials 490 (2017) 247–259.
[22] M. Al Mundheri, P. Soulat, A. Pineau, Irradiation embrittlement of a low alloy steel interpreted in terms of a local approach of cleavage fracture, Fatigue Fract. Engng. Mater. Struct. 12 (1989) 19–30.
[23] K. Wallin, Irradiation damage effects on the fracture toughness transition curve shape for reactor pressure vessel steels, Int. J. Pres. Ves. and Piping 55 (1993) 61–79.
[24] F. Beremin, A local criterion for cleavage fracture of a nuclear pressure vessel steel, J. Metall. Trans. A 14A (1983) 2277–2287.
[25] A. Pineau, B. Tanguy, Advances in cleavage fracture modelling in steels: Micromechanical, numerical and multiscale aspects, Compte Rendus Physique 11 (2010) 316–325.
[26] P. James, M. Ford, A. Jivkov, Predictions of fracture toughness for weld material when adopting a novel particle failure criterion and a measured experimental particle distribution, Vol. ASME Pressure Vessels and Piping Conference, 2013.
[27] P. James, M. Berveiller, Fracture toughness predictive models within the SOTERIA EU project, Vol. ASME Pressure Vessels and Piping Conference, 2018.
[28] A. Gurson, Continuum theory of ductile rupture by void nucleation and growth: Part I - Yield criteria and flow rules for porous ductile media, J. Eng. Mat. and Tech. 99 (1977) 2–15.
[29] V. Tvergaard, On localization in ductile materials containing spherical voids, Int. J. Frac. 18 (1980) 237–252.
[30] V. Tvergaard, A. Needleman, Analysis of the cup-cone fracture in a round tensile bar, Acta Metall. 52 (1984) 157–169.
[31] A. A. Benzerga, J.-B. Leblond, Ductile fracture by void growth to coalescence, Adv. Applied Mech. 44 (2010) 169–305.
[32] A. Benzerga, J. Leblond, A. Needleman, V. Tvergaard, Ductile failure modeling, Int. J. Frac. 201 (2016) 29–80.
[33] D. Norris, Computer simulation of the Charpy V-Notch toughness test, Engineering Fracture Mechanics 11 (2) (1979) 261–274.
[34] K. K. Mathur, A. Needleman, V. Tvergaard, 3D analysis of failure modes in the Charpy impact test, Modelling and Simulation in Materials Science and Engineering 2 (3A) (1994) 617–635.
[35] A. Benzerga, V. Tvergaard, A. Needleman, Size effects in the Charpy V-Notch test, Int. J. Frac. 116 (2002) 275–296.
[36] B. Tanguy, J. Besson, R. Piques, A. Pineau, Ductile to brittle transition of an A508 steel characterized by Charpy impact test: Part II: modeling of the Charpy transition curve, Engineering Fracture Mechanics 72 (3) (2005) 413–434.
[37] C. Bouchet, B. Tanguy, J. Besson, S. Bugat, Prediction of the effects of neutron irradiation on the Charpy ductile to brittle transition curve of an A508 pressure vessel steel, Computational Materials Science 32 (3) (2005) 294–300, iWCMM.
[38] A. Parrot, P. Forget, A. Dahl, Evaluation of Fracture Toughness From Instrumented Charpy Impact Tests for a Reactor Pressure Vessel Steel, Vol. Fatigue, Fracture, and Damage Analysis of Pressure Vessels and Piping Conference, 2003, pp. 1–8.
[39] B. Tanguy, C. Bouchet, S. Bugat, J. Besson, Local approach to fracture based prediction of the ΔT56J and ΔTKIc,100 shifts due to irradiation for an A508 pressure vessel steel, Engineering Fracture Mechanics 73 (2) (2006) 191–206.
[40] B. Tanguy, A. Parrot, F. Clémendot, G. Chas, Assessment of Pressure Vessel Steel Irradiation Embrittlement Up to 40 Years Using Local Approach to Fracture Modelling: Application to the French Surveillance Program, Vol. Volume 3: Design and Analysis of Pressure Vessels and Piping Conference, 2011, pp. 701–708.
[41] G. Johnson, J. Hoegfeldt, U. Lindholm, A. Nagy, Response of various metals to large torsional strains over a large range of strain rates - Part 2: Less ductile metals, J. Eng. Mater. Technol. 105 (1983) 48–53.
[42] J. Hure, C. Vaille, P. Wident, D. Moinereau, C. Landron, S. Chapuliot, C. Benhamou, B. Tanguy, Warm PreStress effect on highly irradiated reactor pressure vessel steel, J. Nuc. Mat. 464 (2015) 281–293.
[43] G. Qian, V. Gonzalez-Albuixech, M. Niffenegger, Calibration of Beremin model with the Master Curve, Engineering Fracture Mechanics 136 (2015) 15–25.
[44] B. Margolin, V. Kostylev, Radiation embrittlement modelling for reactor pressure vessel steels: II. Ductile fracture toughness prediction, International Journal of Pressure Vessels and Piping 76 (10) (1999) 731–740.
[45] B. Tanguy, B. Marini, P. Wident, P. Todeschini, P. Joly, RPV fracture toughness of various metallurgical zones at very high fluences, in: Proceedings of Fontevraud 9 Contribution of Materials Investigations and Operating Experience to LWRs' Safety, Performance and Reliability, 2018.
[46] J. Chaboche, A review of some plasticity and viscoplasticity constitutive theories, Int. J. Plast. 24 (2008) 1642–1693.
[47] B. Tanguy, Modélisation de l'essai Charpy par l'approche locale de la rupture: application au cas de l'acier 16MND5 dans le domaine de la transition, Ph.D. thesis, Ecole Nationale Supérieure des Mines de Paris (2001).
[48] J. Besson, Continuum models of ductile fracture: a review, Int. J. Dam. Mech. 19 (2010) 3–52.
[49] P. F. Thomason, A three-dimensional model for ductile fracture by the growth and coalescence of microvoids, Acta. Metall. 33 (1985) 1087–1095.
[50] L. Cheng, K. Danas, A. Constantinescu, D. Kondo, A homogenization model for porous ductile solids under cyclic loads comprising a matrix with isotropic and linear kinematic hardening, International Journal of Solids and Structures 121 (2017) 174–190.
[51] M. Torki, A. Benzerga, J. Leblond, On void coalescence under combined tension and shear, J. Appl. Mech. 82 (2015) 071005.
[52] T. Helfer, B. Michel, J. Proix, M. Salvo, J. Sercombe, M. Casella, Introducing the open-source mfront code generator: Application to mechanical behaviours and material knowledge management within the pleiades fuel element modelling platform, Computers & Mathematics with Applications 70 (2015) 994–1023.
[53] C. Miehe, N. Apel, M. Lambrecht, Anisotropic additive plasticity in the logarithmic strain space: modular kinematic formulation and implementation based on incremental minimization principles for standard materials, Computer methods in Applied mechanics and engineering 191 (2002) 5383–5425.
[54] M. Shokeir, J. Hure, T. Helfer, Extension of the standardelastoviscoplasticity brick to porous materials, https://www.researchgate.net/publication/346484549_Extension_of_the_StandardElastoViscoPlasticity_brick_to_porous_materials.
[55] CEA, Cast3M, www-cast3M.cea.fr.
[56] T. Byun, N. Hashimoto, Strain localization in irradiated materials, Nuc. Eng. Tech. 38 (2006) 619–638.
[57] J. Faleskog, X. Gao, C. Shih, Cell model for nonlinear fracture analysis I. Micromechanics calibration, International Journal of Fracture 89 (1998) 355–373.
[58] L. Morin, J.-C. Michel, Void coalescence in porous ductile solids containing two populations of cavities, European Journal of Mechanics - A/Solids 72 (2018) 341–353.